



Sr and Zr diffusion in LSCF/10GDC/8YSZ triplets for solid oxide fuel cells (SOFCs)



Fangfang Wang^{a,*}, Mina Nishi^a, Manuel E. Brito^b, Haruo Kishimoto^a, Katsuhiko Yamaji^a, Harumi Yokokawa^{a,c}, Teruhisa Horita^a

^a Fuel Cell Group, National Institute of Advanced Industrial Science and Technology, Higashi, 1-1-1, AIST Tsukuba Central 5, Tsukuba, Ibaraki 305-8565, Japan

^b Clean Energy Research Center, University of Yamanashi, Takeda 4, Kofu, Yamanashi, 400-8510, Japan

^c Institute of Industrial Science, The University of Tokyo, Komaba 4-6-1, Meguro-Ku, Tokyo, 153-8505, Japan

HIGHLIGHTS

- SrZrO₃ is formed along both the LSCF/10GDC and the 10GDC/8YSZ interfaces.
- Zr diffusion along grain boundary of the 10GDC interlayer is fast.
- The chemical potential gradient inside the 10GDC interlayer causes these cations diffusion.

ARTICLE INFO

Article history:

Received 31 August 2013

Received in revised form

12 January 2014

Accepted 11 February 2014

Available online 20 February 2014

Keywords:

Strontium

Zirconium

Diffusion

SrZrO₃

10GDC interlayer

SOFC

ABSTRACT

In this work we attempt to give solution to apparently inconsistent results on grain boundary diffusion of Sr in 10GDC that we have found in our earlier diffusion experiments. The emphasis is placed on using of diffusion triplets: LSCF(porous)/10GDC(dense)/8YSZ(dense) that reproduce the driving forces for Sr diffusion found in solid oxide fuel cell (SOFC) real systems. The diffusion triplets were annealed at 1100 and 1200 °C for one week. Detailed analyses of the microstructure and elemental distributions unequivocally demonstrate the SrZrO₃ formation along both the LSCF/10GDC and the 10GDC/8YSZ interfaces as the result of strontium and zirconium counter directional grain boundary diffusion through the 10GDC interlayer. Furthermore, micro-cracks in the 10GDC interlayer, formed during pre-annealing of the 10GDC/8YSZ layers, were also found to contribute to the SrZrO₃ formation via surface diffusion. Thermodynamic considerations taking in account these microstructural features successfully explain, in terms of the chemical potential gradients developed across the 10GDC layer, why SrZrO₃ is formed along both interfaces when grain boundary diffusion, or surface diffusion (along crack walls), become dominant compared to bulk diffusion through the 10GDC.

© 2014 Elsevier B.V. All rights reserved.

1. Introduction

In solid oxide fuel cells (SOFCs), the cell performance is negatively affected by the formation of non-conducting reaction products at the cathode/electrolyte interfaces. The formation of La₂Zr₂O₇ along the lanthanum manganite/yttrium stabilized zirconia interface is well documented in both theoretical [1,2] and experimental works [3–5]. A slightly different and less studied phenomenon is seen in the SrZrO₃ formation at interfaces between, for example, the lanthanum strontium cobalt iron oxides (LSCF)

cathode and the yttria stabilized zirconia (YSZ) electrolyte. To mitigate the zirconate formation, a diffusion barrier consisting mainly of rare-earth doped ceria (such as Gd_{0.1}Ce_{0.9}O_{1.95}) was proposed in the seminal work by Uchida et al. [6], and other many groups have followed it by applying the doped ceria interlayer to LSCF or similar cathodes in YSZ electrolyte systems [7–13]. Nevertheless, the SrZrO₃ formation seems to be still a problem when GDC is used as a diffusion barrier [8–13]. For this reason and to further understand the strontium (Sr) transport behavior across the GDC layer, we have devoted intensive experimental work [14–18]. At this point, three different diffusion paths have been identified when using industrial scale produced porous GDC layer: (i) grain boundary diffusion, (ii) surface diffusion along pore walls, and (iii) gas diffusion. Our first attempts on this matter [14,15] were

* Corresponding author. Tel.: +81 29 861 3387; fax: +81 29 861 4540.

E-mail addresses: ysdyj8023@yahoo.co.jp, wan.fangfang@aist.go.jp (F. Wang).

made using diffusion couples between perovskite cathode pellets and rare-earth doped ceria pellets somehow loosely winded with platinum wires. Secondary ion mass spectrometric (SIMS) results showed concentration profiles of Sr in ceria, allowing the determination of diffusion coefficients of Sr in both bulk and along grain boundaries. Interestingly enough, SIMS and related analyses indicate that transition elements (Co, Fe) in cathodes tend strongly to diffuse into ceria layers to form compounds with dopants such as Gd or La. Needless to say that Sr diffusion should be also affected by the diffusional behavior of transition metal ions. Since mass transfer of transition metal ions should be accompanied with their valence changes, two main factors are considered to affect mass transport in those experiments: (i) the presence of air between the mating pellet surfaces and (ii) a possible effects of catalytic activity of platinum, which can migrate to the interfaces as gaseous species. Thus, to eliminate such possible effects of gaseous phases at the interface, a dense LSCF layer was deposited on 10GDC pellets by the pulsed laser deposition (PLD) technique; and using similar techniques, the cation diffusion from the dense LSCF film toward the dense sintered 10GDC was investigated. [16] Surprisingly, while the bulk and grain boundary diffusions of Sr, Fe, and Co were not detected clearly, both bulk and grain boundary diffusions of La into the dense sintered 10GDC were notably observed. Furthermore, similar results were obtained even when a porous LSCF was used [18].

In principle, our results are in agreement with recently published data pointing out the positive role of dense GDC as an effective diffusion barrier [8–10]. Even so, our primary objective still is to determine the bulk or grain boundary diffusion coefficients of Sr in GDC. It is known that Sr diffusion takes place to form SrZrO_3 at the GDC/YSZ interfaces in real cell environments, a new diffusion experiment was designed to basically reproduce the driving forces for SrZrO_3 formation found in real systems; thus, a diffusion “triplet” was prepared consisting of LSCF (porous)/10GDC (dense)/8YSZ (dense) layers. Diffusion triplets were heat-treated and analyzed in the same way we did for diffusion couples to evaluate cation diffusion across the ceria interlayer. The SIMS diffusion profiles exhibited complicated features, and supplementary detailed analyses of the microstructure were made by scanning electron microscopy (SEM) and energy dispersive X-ray spectroscopy (EDX). Since the SrZrO_3 formation was observed not only at the interfaces between 10GDC/8YSZ but also between LSCF/8YSZ, the role of the interlayer microstructural features on the magnitude of Sr and Zr diffusion is discussed in a qualitative manner.

2. Experimental

A pulsed laser deposition (PLD) target and substrates were prepared using $\text{Gd}_{0.1}\text{Ce}_{0.9}\text{O}_{1.95}$ (10GDC, Anan Kasei Co., Ltd., Japan) powers and 8 mol% Y_2O_3 -stabilized ZrO_2 (8YSZ, TZ-8Y, Tosoh Co., Ltd., Japan) powders, respectively. The 10GDC powders were shaped into a large disk (25 mm in diameter and 5 mm thick) and the 8YSZ powders were shaped into small disks (15 mm in diameter and 1 mm thick). The pressed disks were further cold-isostatically pressed at 390 MPa. The sintering temperature was selected at 1400 °C for both 10GDC and 8YSZ.

Experiments of PLD were performed as follows. In a vacuum chamber with 10 Pa of oxygen partial pressure, a pulsed KrF ($\lambda = 248$ nm) excimer laser was focused onto the rotating polycrystalline target of 10GDC. The laser pulse energy and the repetition rate were 200 mJ and 10 Hz, respectively. The ablated 10GDC substrate emitted a plume in direction normal to its surface and depositing onto the 8YSZ substrate heated at 650 °C, followed by pre-annealing at 1300 °C for 5 h to homogenize the PLD deposited film. The thickness of the deposited 10GDC film was approximately

5 μm . A diffusion triplet was then completed by screen printing of $\text{La}_{0.8}\text{Sr}_{0.2}\text{Co}_{0.2}\text{Fe}_{0.8}\text{O}_{3-\delta}$ (LSCF8228) or $\text{La}_{0.6}\text{Sr}_{0.4}\text{Co}_{0.2}\text{Fe}_{0.8}\text{O}_{3-\delta}$ (LSCF6428) (AGC Seimi Chemical Co., Ltd., Japan) on the 10GDC film. The powder size of LSCF6428 and LSCF8228 was 0.5 μm . The diffusion triplet samples of LSCF/10GDC/8YSZ were annealed at 1100 °C or 1200 °C for 168 h in air at a flowing rate of 50 $\text{cm}^3 \text{min}^{-1}$.

Crystalline phases involved in this study were identified by standard X-ray diffractometry (XRD, Ultima IV, Rigaku Co., Japan). The cross-sectional studies were performed using scanning electron microscopy (FE-SEM, JSM-7001, JEOL, Japan) and energy dispersive X-ray spectroscopy (EDX, INCA, Oxford, England) analysis. Elemental distribution as a function of depth was obtained using secondary ion mass spectrometer (SIMS, 5f, Cameca, France). The sample surface was impinged by focused Cs^+ ions (accelerating voltage = 10 kV) and the emissions from the surface were detected as negative secondary ions. The intensities of secondary ions $^{16}\text{O}^-$, $^{18}\text{O}^-$, M^{16}O^- (where $\text{M} = ^{56}\text{Fe}$, ^{59}Co , ^{88}Sr , ^{139}La , ^{140}Ce , ^{158}Gd , ^{90}Zr , and ^{89}Y) were collected as a function of etching time. The samples were coated with a gold thin film to avoid charging effects and the analysis was always made under electron irradiation for the same purpose, especially when the profiles reach the “insulator” 10GDC. The crater depth of etched area was measured by a surface profiler (Ultra-deep Color 3D Profile Measuring Microscope, VK-9510, Keyence Co., Japan).

3. Results and discussion

3.1. Pre-annealing at 1300 °C

Efforts were made to prepare a dense 10GDC interlayer to accurately examine the Sr diffusion behavior. However, in fact, some fine cracks (marked by arrows in Fig. 1) developed perpendicular to the interface in the 10GDC layer after the pre-annealing and appeared in regular intervals of 10–30 μm . A typical fine crack was enlarged as shown in the inset of the Fig. 1b. Bearing in mind the presence of such fine cracks, we have discussed our experimental results for the Sr diffusion.

Fig. 2 shows the elemental distribution of the combined 10GDC/8YSZ layer measured by SIMS for (a) as deposited and (b) after the pre-annealing, respectively. As shown in Fig. 2a, the intensity of Ce and Zr decreases sharply at the 10GDC/8YSZ interface, suggesting essentially no cation diffusion across the interface before the pre-annealing. For the 10GDC/8YSZ after the pre-annealing at 1300 °C for 5 h (see Fig. 2b), we observed two kinds of the behaviors (i) not very steep decrease in intensity of Ce and Gd at the 10GDC/8YSZ interface and (ii) a hump for the Zr and Y profiles within the 10GDC film. At first glance, these behaviors can be attributed to the formation of GDC–YSZ solid solutions. However, close examinations of the SIMS profile reveal that the tails of Ce and Gd inside 8YSZ do not extend to deep regions, suggesting that diffusion of such ions is quite small in magnitude and short in length (about 200 nm). It is also known that at high temperatures, GDC–YSZ solid solutions can be easily formed by the Ce component diffusion into YSZ across the GDC (dense)/YSZ (dense) interfaces leaving Kirkendall pores in the GDC side. [19] The behavior (i) is attributed to a limited amount of formed GDC–YSZ solid solutions. Since Zr can diffuse in YSZ bulk or through grain boundaries, [20] the behavior (ii) can be interpreted in terms of slight deformation of 8YSZ which must take place during the crack formation in the pre-annealing in the vicinity of cracks inside the deposited 10GDC layer. Here, it is important to confirm that the surface diffusion of Zr or Y along the 10GDC crack wall surface seems to be quite small given that the profiles of Zr and Y decrease sharply, in a similar manner to those before the pre-annealing, and in a different manner if compared with the typical grain boundary diffusion or surface diffusion profiles. Note that the

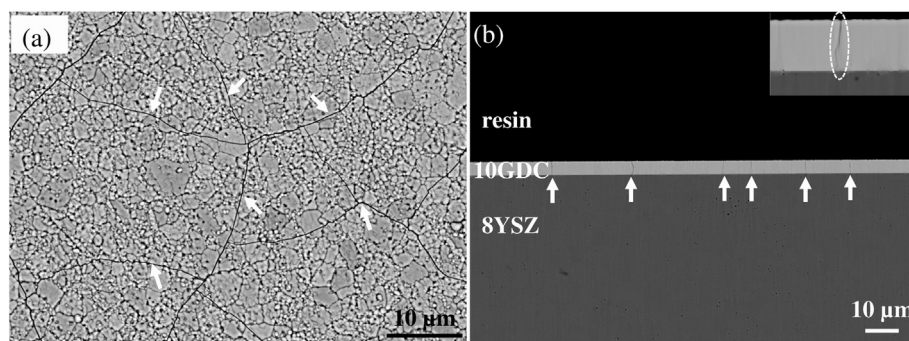


Fig. 1. Backscattered electron images of the 10GDC/8YSZ after pre-annealing at 1300 °C for 5 h; (a) 10GDC surface; (b) cross-section of 10GDC/8YSZ. White arrows: fine cracks within the 10GDC interlayer. Insert: cracks within the 10GDC interlayer in enlarged scale.

thickness of Zr-containing part in 10GDC is much less than 2 μm . The rest of the 10GDC interlayer with the thickness of more than 3 μm is not affected by Zr or Y diffusion. Under these known conditions, the annealing experiments were performed and the Sr transport behavior was investigated.

3.2. Diffusion triplet experiments

Fig. 3 shows backscattered electron images of cross-sections for all the LSCF/10GDC/8YSZ triplets annealed at different temperatures: (a) 1200 °C and (b) 1100 °C for LSCF6428; (c) 1200 °C and (d) 1100 °C for LSCF8228. Although LSCF6428 and LSCF8228 with the same particle size were used, the microstructure was different after the annealing processes; LSCF6428 showed a more significant sintering behavior than that of LSCF8228. Fig. 3a shows the formation of grey spots (indicated by black arrows) at the 10GDC/8YSZ and the LSCF6428/10GDC interfaces. Spikes of this grey phase were also observed inside the 10GDC interlayer. Interestingly enough, the intervals of the grey spikes were about 10–30 μm , which is consistent with the intervals of the cracks observed in 10GDC after

the pre-annealing shown in Fig. 1. The amount and size of the grey spots decreased with decreasing annealing temperature from 1200 to 1100 °C (Fig. 3b). According to Fig. 3a and c, the amount of the grey spots decreased significantly with decreasing Sr concentration in the LSCF cathodes. This suggests that the grey spots were easily formed in LSCF6428 compared with LSCF8228 because of the higher chemical potential values of the Sr component in LSCF6428 [21] and also of the higher Sr diffusion in LSCF6428 that is suggested from the well-sintered microstructure given in Fig. 3. It was reported that the SrZrO_3 is formed at the GDC/YSZ interface in LSCF/GDC/YSZ system [8–10], however, the grey spots were firstly observed at the LSCF/10GDC interface rather than at the 10GDC/8YSZ interface in this work. Since these grey spots were very fine, for the sake of clarity, the spots are shown as the dashed circle inside the enlarged insert of the Fig. 3d. Another interesting behavior should be also noticed, that is, those cracks formed within the 10GDC during the pre-annealing (see Fig. 1b) disappeared after the annealing at 1100 °C (Fig. 2b and d).

To investigate the composition of those grey spots, SEM/EDX analyses for these four diffusion triplets were carried out. Fig. 4a presents typical results of EDX elemental mapping for LSCF6428/10GDC/8YSZ annealed at 1200 °C for 168 h and Fig. 4b shows the point analysis results of the grey point (marked by white arrow). Results for the spikes of grey phase within the 10GDC interlayer and the grey spots along the 10GDC/8YSZ or the LSCF/10GDC interfaces show that Sr, Zr, and O coexisted and there were essentially no other elements. According to the point analysis of these grey spots (Fig. 4b) and spikes of grey phase, the ratio of Sr and Zr was about 1:1, which suggests the formation of SrZrO_3 . The $\text{La}_2\text{Zr}_2\text{O}_7$ formation was not observed in this work.

The annealed samples were soaked in dilute nitric acid (HNO_3) to remove the LSCF porous film. To collect the information of the sample, the 10GDC surface was examined by grazing incidence X-ray diffraction with incidence angular of 10° as shown in Fig. 5. The main reflection lines correspond to 10GDC and 8YSZ. Moreover, the peaks arising from SrZrO_3 were observed for all samples. The intensity of SrZrO_3 peaks became stronger with increasing annealing temperature from 1100 to 1200 °C. At the same annealing temperature, the peak intensity became stronger with increasing Sr concentration in the LSCF cathodes. Some weak peaks can be identified as the $\text{La}_{0.6}\text{Sr}_{0.4-x}\text{FeO}_3$ phase for the LSCF6428/10GDC/8YSZ triplet annealed at 1200 °C, whereas CoFe_2O_4 or Co_3O_4 peaks with weak intensity were observed in the same sample annealed at 1100 °C.

The EDX elemental mapping of the 10GDC surface after removal of LSCF6428 was shown in Fig. 6(a) for the diffusion triplet annealed at 1200 °C and (b) at 1100 °C. At 1200 °C in Fig. 6a, the La and the Fe components were enriched in the same area as the SrZrO_3 phase. At

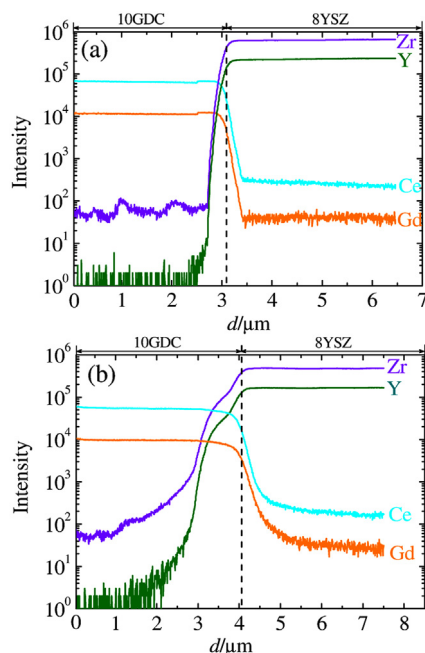


Fig. 2. SIMS depth profiles of the 10GDC/8YSZ; (a) as deposited and (b) after pre-annealing at 1300 °C for 5 h.

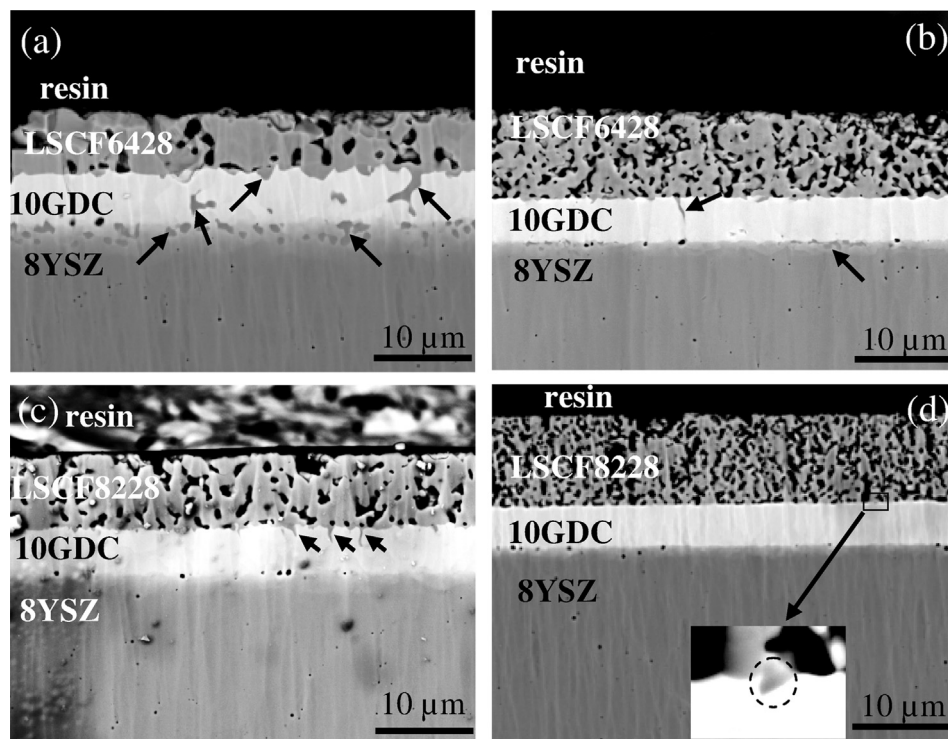
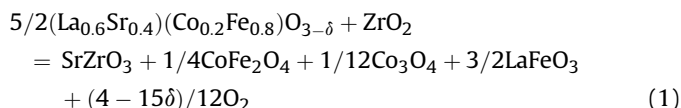


Fig. 3. Backscattered electron images of cross-section of triplets annealed under different temperatures: (a) 1200 °C and (b) 1100 °C for LSCF6428/10GDC/8YSZ; (c) 1200 °C and (d) 1100 °C for LSCF8228/10GDC/8YSZ. Black arrows: grey spots at the LSCF/10GDC and 10GDC/8YSZ interfaces. Insert: enlarged grey spot at the LSCF/10GDC interface.

1100 °C, on the other hand, a Co-rich region was observed and some amount of Fe also appeared in the same region. It confirms that the $\text{CoFe}_2\text{O}_4/\text{Co}_3\text{O}_4$ formation in good correspondence with the XRD results. Those results can be explained as follows: the Sr component at the A sites in the perovskite LSCF diffused to the 10GDC/8YSZ interface and formed SrZrO_3 . Concurrently, the Co and Fe components at the B sites, now in excess within the perovskite lattice, react to form simpler oxides CoFe_2O_4 and Co_3O_4 to keep the mass balance. The reaction equation can be given by



In Fig. 6b, no distribution of La and Fe is observed on the 10GDC surface, suggesting that the LaFeO_3 component in the above reaction was present in the LSCF-derived perovskite phase and therefore was dissolved into the acid. At 1200 °C, however, the La and Fe components remained in the non-dissolved side, suggesting that this LaFeO_3 component forms solid solutions with the SrZrO_3 phase at the LSCF/10GDC interface, and as a result, may become less soluble to the acid.

Fig. 7 shows results by SIMS on elemental distribution in the LSCF6428/10GDC/8YSZ triplet annealed at different temperatures, (a) for 1200 °C and (b) for 1100 °C. Several interesting features can be derived.

- (1) The Sr component diffused from LSCF toward 8YSZ through 10GDC. The clear Sr peak at the 10GDC/8YSZ interface confirms the SrZrO_3 formation at the interface. Diffusion of Co, Fe, and La was observed through the 10GDC interlayer to the 8YSZ side; at 1200 °C, the Co concentration inside 8YSZ is much higher than that annealed at 1100 °C and

correspondingly the Co concentration is much lower in the LSCF phase; this suggests that Co easily diffuses across the 10GDC layer into the 8YSZ at 1200 °C. This provides the reason for why the Co concentrating area is not observed in the LSCF side in Fig. 6a for 1200 °C.

- (2) Moreover, the Zr peak at the LSCF/10GDC interface also proved the SrZrO_3 formation in this region. This provides some evidence for the Zr diffusion across the 10GDC interlayer in contrast to the pre-annealing in which the Zr diffusion on the crack walls is not detected. This is probably because the presence of Co, Fe, Sr or SrZrO_3 on the walls enhances the diffusion of Zr.
- (3) Although the SrZrO_3 phase is formed at the both sides of the 10GDC layer, features inside the 10GDC layer are different; at 1200 °C, there appear SrZrO_3 phases inside the 10GDC layer, while essentially no formation of SrZrO_3 at 1100 °C. Interesting features can be seen in the concentration profiles of Co, Fe, La which exhibit similar trends of the Sr concentration profiles. This indicates that those elements are also some solubility into the SrZrO_3 phase, whereas in 8YSZ, the solubility of Sr and La is limited so that no long diffusion tails are observed, while Co and Fe diffused deep inside 8YSZ.
- (4) Effects of Co, Fe can be also recognized in the feature that at 1200 °C, those cracks which were formed during the pre-annealing disappeared apparently due to enhanced sintering of 10GDC in the presence of a small amount of Co and Fe [22,23].
- (5) The Gd component in the 10GDC layer was lowered in concentration and mainly diffused into the LSCF layer for both 1100 °C and 1200 °C. In the 8YSZ side, the concentration tails of the Gd and Ce components are closely related with the Sr component, suggesting that the SrZrO_3 phase contains Ce and Gd as minor components or that the SrZrO_3 phase coexists with the 10GDC phase to form the two-phase zone between the 10GDC and the 8YSZ layers. Fig. 4 indicates that the Ce

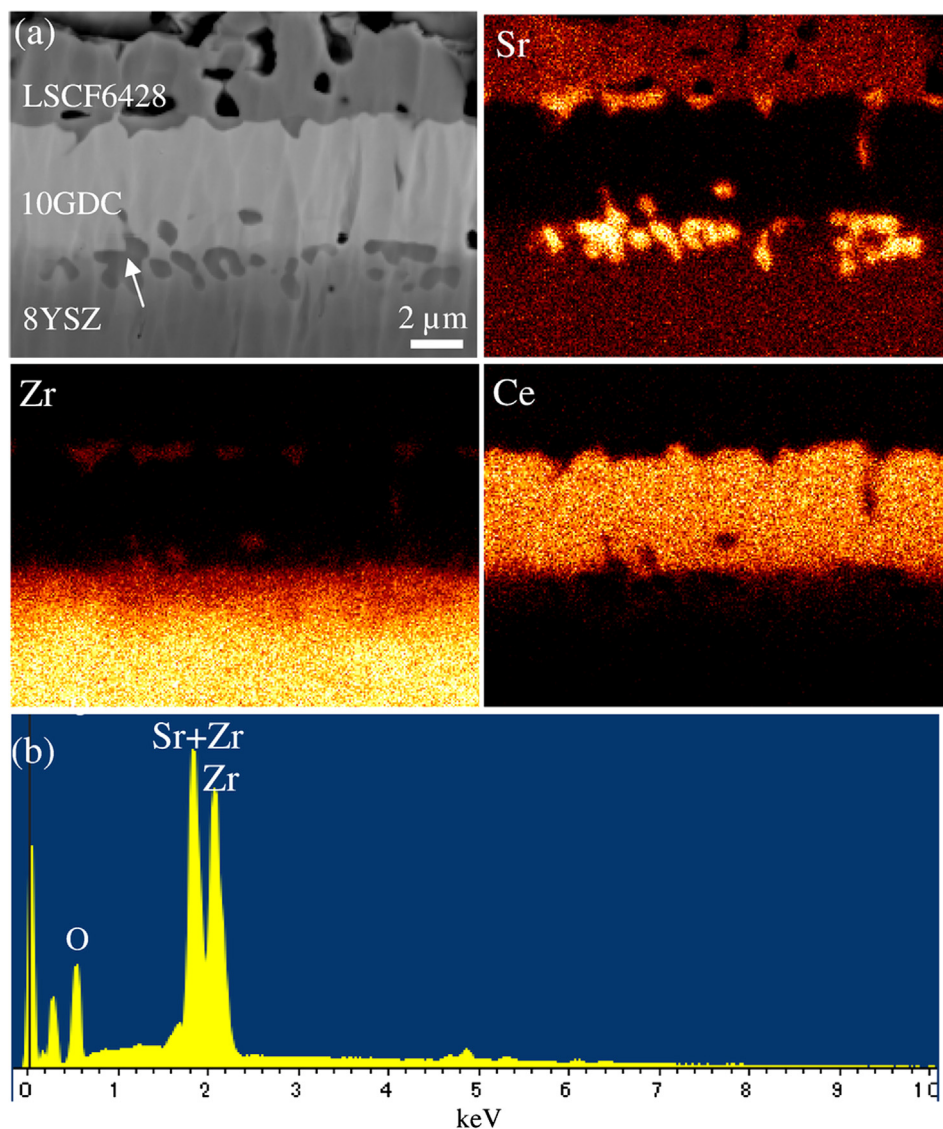


Fig. 4. (a) A typical EDX mapping of LSCF6428/10GDC/8YSZ annealed at 1200 °C for 168 h, and (b) point analysis of the grey point shown by white arrow.

component in the 8YSZ rich area is located mainly in the SrZrO_3 region, suggesting those Ce and Gd components tend to exist as a part of the GDC–YSZ solid solutions. In particular, the Gd profile at 1200 °C can be well interpreted by the normal inter-diffusion profile that the rare-earth element tends to migrate from the ceria side to the zirconia side [19].

3.3. Short summary of experimental observations

Based on the above results, the Sr and related Zr diffusion behaviors are schematically summarized in Fig. 8 and Table 1. In this table, the sintering process of 10GDC/8YSZ during the pre-annealing is included as sequence No. 1. In this step, there is essentially no Zr diffusion within the 10GDC interlayer. Our previous results have shown that the Sr bulk diffusion length in the 10GDC is less than 0.5 μm for the present annealing condition [16]; since this length is much shorter than the thickness of the 10GDC interlayer (~5 μm), the bulk diffusion of Sr in 10GDC should be negligible in the present cases. There are thus two possible Sr

diffusion paths in the 10GDC layer: (1) surface (or gaseous) diffusion inside cracks and (2) grain boundary diffusion as shown in Fig. 8b.

The diffusion and related fluxes can be divided into the following two cases.

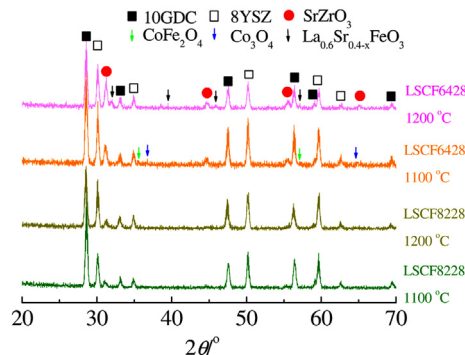


Fig. 5. XRD patterns of 10GDC surface after removal of LSCF from triplets of LSCF/10GDC/8YSZ annealed under different temperatures.

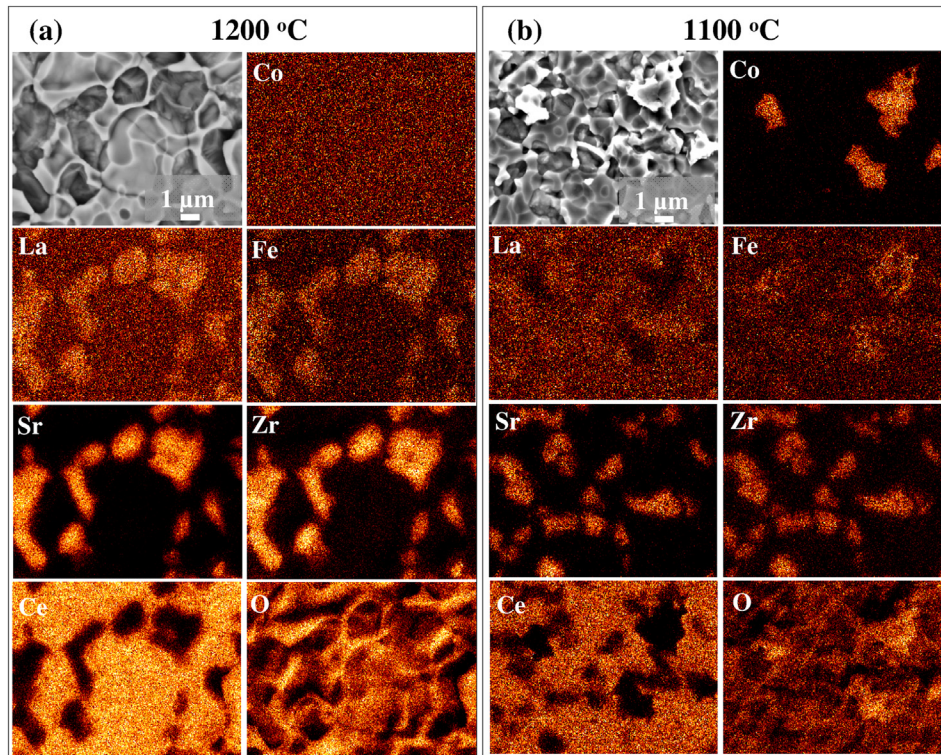


Fig. 6. EDX mapping of 10GDC surface after removal of LSCF6428 from triplets of LSCF6428/10GDC/8YSZ annealed at (a) 1200 °C and (b) 1100 °C.

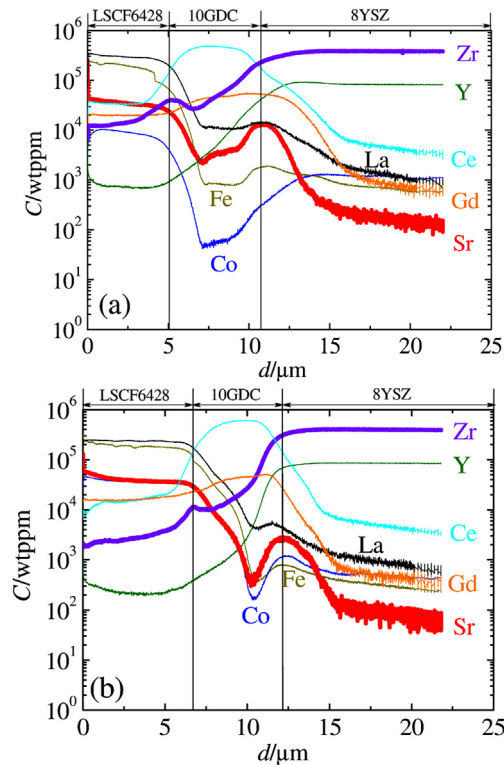


Fig. 7. SIMS depth profile of LSCF6428/10GDC/8YSZ annealed at (a) 1200 °C and (b) 1100 °C.

3.3.1. Initial stage: (1100 °C for LSCF8228 and LSCF6428 and 1200 °C for LSCF8228)

SrZrO₃ was formed at both sides of the 10GDC interlayer as described as sequence No. 2 in Table 1. This SrZrO₃ formation includes two parallel diffusion steps (2a and 2b in Table 1). Major parts of SrZrO₃ were formed at the interface between LSCF and 10GDC. This is mainly accelerated by the Zr diffusion through grain boundaries from the 8YSZ side to the LSCF/10GDC interface. Since the Zr diffusion is quite limited during the annealing of the 10GDC–8YSZ couples, this acceleration is due to the presence of the LSCF layer which causes the Co, Fe diffusion into 10GDC. This Zr diffusion was accompanied with Kirkendall pores inside the 8YSZ pellet near to the interface, suggesting that the Zr diffusion through grain boundaries in 10GDC is higher than those in 8YSZ bulk or grain boundaries. The formed SrZrO₃ at the LSCF/10GDC interface grew along the grain boundaries inside 10GDC toward 8YSZ. Even so, the driving forces for further growth may decrease because not a further amount of SrZrO₃ was formed on this side. This is probably related with the CoFe₂O₄ formation which is schematically shown as precipitates at the interfaces in Fig. 8a, where the chemical potential change within this process is shown schematically. To make it clear the driving force for the diffusion involved with SrZrO₃ formation, the chemical potential of SrO, ZrO₂ and SrZrO₃ are plotted. The chemical potential of SrZrO₃ is generally given as a sum of those of SrO and ZrO₂ as follows;

$$\mu(\text{SrO}) + \mu(\text{ZrO}_2) = \mu(\text{SrZrO}_3) \quad (2)$$

Here, $\mu(\text{SrZrO}_3)$ has the maximum value of $\mu(\text{SrZrO}_3)$ when the pure SrZrO₃ phase is present. Along the grain boundary diffusion path, $\mu(\text{SrZrO}_3)$ becomes this maximum at the LSCF/8YSZ interface. Note that $\mu(\text{SrO})$ and $\mu(\text{ZrO}_2)$ vary independently except inside SrZrO₃ phase where Eq. (2) becomes equal to $\mu(\text{SrZrO}_3)$. When Sr diffuses into 10GDC and CoFe₂O₄ is precipitated near to the SrZrO₃ phase,

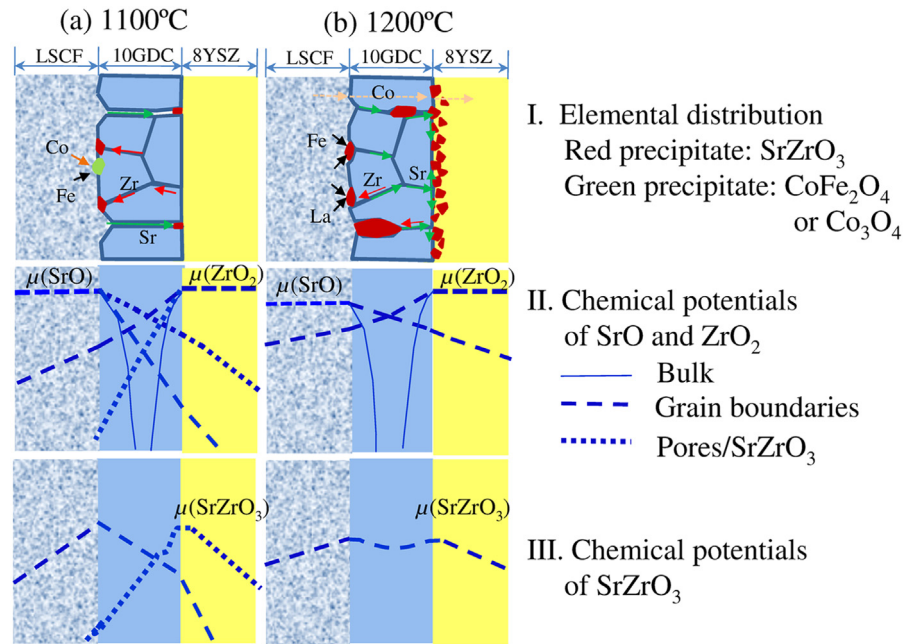


Fig. 8. Schematic element distribution across triplets of LSCF/10GDC/8YSZ annealed at (a) 1100 °C and (b) 1200 °C. The upper graph is for (I) elemental distribution of Sr and Zr, the middle graph is for (II) chemical potential profile of Sr and Zr, and the lower graph is for (III) chemical potential distribution of SrZrO₃.

the chemical potential of SrO decreases to have the lowest value in the region where the LSCF phase exists stably [21], leading to increase in the chemical potential of ZrO₂ at this region. Since the chemical potential of ZrO₂ in 8YSZ is constant at nearly its maximum, the driving force of diffusion, slope of the chemical potential decreases along this diffusion path. This corresponds well to observed features of SrZrO₃.

In addition, a slight amount of SrZrO₃ was formed at the bottom of cracks appearing in 10GDC during the pre-annealing process. This SrZrO₃ formation took place at the 10GDC/8YSZ interface so that the chemical potential of ZrO₂ should initially be around its maximum value in 8YSZ, whereas the chemical potential of SrO has a rather steep slope as shown in Fig. 8. The Sr flux through cracks is larger than that of Zr through cracks but is small in magnitude. For this SrZrO₃ phase growth, the supply of both Sr and Zr is needed; the Sr is supplied through cracks, whereas the Zr diffuses from 8YSZ. Although the growing direction is not well clarified; it is suggested from other similar processes to be discussed in the next stage, the Sr

diffusion seems to be faster in SrZrO₃ than Zr. In such a case, the Sr flux through the cracks limits the rate of the SrZrO₃ growth.

3.3.2. Second stage: 1200 °C for LSCF6428

SrZrO₃ grew from the LSCF/10GDC interface to the 10GDC/8YSZ interface (sequence No. 3), extended along the 10GDC/8YSZ interface (sequence No. 4) and finally entered into 8YSZ (sequence No. 5 in Table 1). This stage can be characterized as substantial cation diffusion from the LSCF side to the 8YSZ side. For example, the Co component decreases in concentration at the LSCF/10GDC interface and increases at the 10GDC/8YSZ interface or inside 8YSZ. Since the Co component in 10GDC or 8YSZ enhances sintering, pores in 8YSZ as well as cracks in 10GDC essentially disappear. A larger amount of SrZrO₃ is now formed at the 10GDC/YSZ interfaces than at the LSCF/10GDC interface. Since cracks already disappear, that is, partly become pores or are partly eliminated, there remains only grain boundary diffusion path in 10GDC. Along this path, the Sr component is transferred in a more enhanced manner compared with

Table 1

Summaries of considerations on diffusion of Sr and Zr in various plausible diffusion paths.

Chronological sequence no. and process involved	Plausible paths	Diffusing species	Relative diffusivity	Temperature (°C)	Remarks
1. No Zr diffusion in 10GDC	10GDC GBs	Zr diffusion in 10GDC	$D(\text{Zr, GBs } 10\text{GDC})$ nearly zero	1300	Essentially no Zr diffusion in 10GDC
2a. SrZrO ₃ formation I	10GDC GBs with Co/Fe	Enhanced Zr diffusion at GBs	$D(\text{Zr, GBsw}) > D(\text{Sr, GBsw})$	1100–1200	SrZrO ₃ formation at the LSCF/10GDC interface
2b. SrZrO ₃ formation II	Surfaces of 10GDC cracks	Sr supply through cracks	$D(\text{Sr, crack}) > D(\text{Zr, crack})$	1100–1200	SrZrO ₃ formation at the 10GDC/8YSZ interface
3. Growth of SrZrO ₃ I	a. 10GDC GBs with Co/Fe b. SrZrO ₃ or interface with 10GDC	Supply of Zr from YSZ side Supply of Sr from LSCF side	$D(\text{Zr, GBsw}) > D(\text{Sr, GBsw})$ $D(\text{Sr, SZ}) > D(\text{Zr, SZ})$	1100–1200 1100–1200	Growth of SrZrO ₃ from LSCF interface to 10GDC side
4. Growth of SrZrO ₃ II	Growth of SrZrO ₃ at 10GDC/8YSZ interface	Supply of Sr through formed SrZrO ₃ , gb	$D(\text{Sr, gb or SZ}) > D(\text{Zr, gb or SZ})$	1200	Growth of SrZrO ₃ to the 10GDC/8YSZ interface
5. Growth of SrZrO ₃ III	Growth of SrZrO ₃ at 10GDC/8YSZ interface	Supply of Sr through 8YSZ GBs	$D(\text{Sr, GBs } 8\text{YSZ})$	1200	Growth from the 10GDC/8YSZ interface to 8YSZ side

GBs = Grain boundaries; GBsw = 10GDC grain boundaries with Co/Fe; gb = 10GDC grain boundaries with wider width; and SZ = inside SrZrO₃ or its interface with 10GDC.

those in No. 2a. This is probably because of the higher annealing temperature which causes more significant diffusion through 10GDC; that is, a larger amount of Co, Fe, La components are present along the grain boundaries and this may make grain boundaries widened with changes in their ionic arrangement similar to that of the perovskite lattice.

The chemical potential distribution along the diffusion path is also shown in Fig. 8b; SrZrO₃ appears at both sides of 10GDC so that the sum of $\mu(\text{SrO})$ and $\mu(\text{ZrO}_2)$ becomes nearly constant around $\mu(\text{SrZrO}_3)$ inside the 10GDC layer. In this situation, from the Eq. (2), the gradient of chemical potentials of SrO and ZrO₂ should be nearly the same in magnitude but opposite in the direction. This indicates that diffusivity of Sr and Zr along the widened grain boundaries in this stage should have the following sequence:

$$D(\text{Sr, gb}) > D(\text{Zr, gb}) \quad (3)$$

where, gb means the grain boundary with the widened and enhanced path as given in Table 1. This is consistent with above discussions that the grain boundary becomes similar to perovskite lattice structure where the A-site elements have generally higher diffusivity than the B-site elements. This difference should be compared with the 10GDC grain boundaries in the earlier stage (Nos. 2a and 3a) in which the following difference appears in diffusivity.

$$D(\text{Zr, GBsw}) > D(\text{Sr, GBsw}) \quad (4)$$

where GBsw means the grain boundaries with Co/Fe in GDC after the annealing of diffusion triplets. This indicates that the grain boundary diffusions of Sr or Zr may change magnitude as a function of an amount of Co or Fe present in grain boundaries. We hope to experimentally confirm this feature.

3.4. Comparison with our earlier experimental results

Compared with our two earlier results which are in conflict with each other, the present results exhibit similarities with the diffusion couples of 10GDC-perovskite pellets [14,15] in the following aspects.

- (1) Both cases exhibit the Sr diffusion in a significant depth inside 10GDC and this is accompanied with the corresponding diffusion of the Co/Fe components of LSCF into the 10GDC or even to the 8YSZ part in the present case as well as with the diffusion of dopant of 10GDC into the perovskite cathode materials.
- (2) In the present case, an anomalous behavior of the La component appeared only in the feature that the LaFeO₃ component is partly dissolved into the formed SrZrO₃ to form solid solutions at 1200 °C.

Since the selective diffusion of the La component into 10GDC which was observed on the PLD LSCF film on 10GDC [16] is not accompanied with other diffusion or compound formation, it is suggested that the formation of the La-dissolved 10GDC thin layer may block other processes. In other words, many dissolutions/diffusion/compound formation processes can proceed simultaneously at different sites or through different diffusion paths. Since the inter-diffusion of the Co/Fe components from the perovskite to the fluorite lattice should be accompanied with changes in their valence number, oxygen incorporation/excorporation should be also involved in those complicated processes.

3.5. Possible other effects

According to the above discussion, the Sr diffusion path across the 10GDC interlayer was determined to be the grain boundary diffusion and surface diffusion. Supposing that a 10GDC interlayer without the cracks could be prepared, the Sr surface diffusion can be avoided. On the other hand, the Sr grain boundary diffusion across the interlayer (for example 10GDC) would never stop. However, the operation temperature of SOFCs is much lower than the present annealing temperature and the diffusion rate becomes quite slow in the operation conditions of SOFCs. In this study, we have just evaluated the Sr diffusion behavior under simple annealing conditions (the OCV condition). However, SOFC real cells/stacks are operated under polarization conditions. The polarization condition causes a change in the oxygen potential distribution within the electrolyte and electrode and it should also affect the cation diffusion behavior across the interlayer. Our group is already engaged in experimental work leading to understand the effect of the polarization on the Sr or Zr diffusion behavior. In a near future we will be able to report on the definitive story of the 10GDC interlayer as a diffusional barrier between cathode and electrolyte.

4. Conclusions

The Sr or Zr diffusion paths were evaluated in diffusion triplets of LSCF/10GDC/8YSZ. Two diffusion paths were identified: grain boundary diffusion and surface diffusion. The surface diffusion is associated with the presence of cracks within the 10GDC interlayer. On the other hand, grain boundary diffusion across the 10GDC interlayer caused the SrZrO₃ formation along the interfaces in both sides of the 10GDC interlayer. We have concluded that although even a dense 10GDC interlayer cannot stop the Sr diffusion, it seems to play a significant role delaying the Sr diffusion and consequently delaying the formation of insulating phases along the cathode/electrolyte interface. In addition, simultaneous detection of Co and Fe in 10GDC by SIMS suggests that the presence of these two elements in the grain boundaries of 10GDC strongly affect the diffusivity of Sr and Zr.

Acknowledgments

The work was financially supported by the New Energy and Industrial Technology Development Organization (NEDO) of Japan.

References

- [1] H. Yokokawa, N. Sakai, T. Kawada, M. Dokiya, J. Electrochem. Soc. 138 (1991) 2719–2727.
- [2] H. Yokokawa, Annu. Rev. Mater. Res. 33 (2003) 581–610.
- [3] S.K. Lau, S.C. Singhal, Corrosion 85 (1985) 1–9. Paper No. 345.
- [4] J.A.M. Van Roosmalen, E.H.P. Cordfunke, J. Solid State Chem. 93 (1993) 212–223.
- [5] K. Kleaveland, M.A. Einarsrud, C.R. Schmidt, S. Shamsili, S. Faaland, K. Wiik, T. Grande, J. Am. Ceram. Soc. 82 (3) (1999) 729–734.
- [6] H. Uchida, S. Arisaka, M. Watanabe, Electrochem. Solid-State Lett. 2 (9) (1999) 428–430.
- [7] J. Peña-Martínez, D. Marrero-López, C. Sánchez-Bautista, A.J. Dos Santos-García, J.C. Ruiz-Morales, J. Canales-Vázquez, P. Núñez, Bol. Soc. Esp. Ceram. 49 (1) (2010) 15–22.
- [8] R. Knibbe, J. Hjelm, M. Menon, N. Pryds, M. Søgaard, H.J. Wang, K. Neufeld, J. Am. Ceram. Soc. 93 (9) (2010) 2877–2883.
- [9] S. Uhlenbruck, T. Moskalowicz, N. Jordan, H.J. Penkalla, H.P. Buchkremer, Solid State Ionics 180 (2009) 418–423.
- [10] N. Jordan, W. Assenmacher, S. Uhlenbruck, V.A.C. Haanappel, H.P. Buchkremer, D. Stöver, W. Mader, Solid State Ionics 179 (2008) 919–923.
- [11] A. Mai, V.A.C. Haanappel, S. Uhlenbruck, F. Tietz, D. Stöver, Solid State Ionics 176 (2005) 1341–1350.
- [12] A. Mai, M. Becker, W. Assenmacher, F. Tietz, D. Hathiraman, E. Ivers-Tiffée, D. Stöver, W. Mader, Solid State Ionics 177 (2006) 1965–1968.

- [13] W.H. Kim, H.S. Song, J. Moon, H.W. Lee, *Solid State Ionics* 177 (2006) 3211–3216.
- [14] N. Sakai, H. Kishimoto, K. Yamaji, T. Horita, M.E. Brito, H. Yokokawa, *J. Electrochem. Soc.* 154 (12) (2007) B1331–B1337.
- [15] N. Sakai, H. Kishimoto, K. Yamaji, T. Horita, M.E. Brito, H. Yokokawa, *ECS Trans.* 1 (2007) 389–398.
- [16] M. Izuki, M.E. Brito, K. Yamaji, H. Kishimoto, D.H. Cho, T. Shimonosono, T. Horita, H. Yokokawa, *J. Power Sources* 196 (2011) 7232–7236.
- [17] F. Wang, M.E. Brito, K. Yamaji, T. Shimonosono, M. Nishi, D.H. Cho, H. Kishimoto, T. Horita, H. Yokokawa, in: *Proceeding of the Tenth European SOFC Forum*, 2012, p. B0512.
- [18] M. Izuki, M.E. Brito, K. Yamaji, H. Kishimoto, T. Shimonosono, D.H. Cho, F. Wang, T. Horita, H. Yokokawa, in: *Extended Abstract of the 15th Symposium on Solid Oxide Fuel Cells in Japan*, 2010, p. 164C.
- [19] K. Eguchi, N. Akasaka, H. Mitsuyasu, Y. Nonaka, *Solid State Ionics* 135 (2000) 589–594.
- [20] M.A. Taylor, M. Kilo, G. Borchardt, S. Weber, H. Scherrer, *J. Eur. Ceram. Soc.* 25 (2005) 1591–1595.
- [21] H. Yokokawa, N. Sakai, T. Horita, K. Yamaji, M.E. Brito, H. Kishimoto, *J. Alloy. Compd.* 452 (2008) 41–47.
- [22] C.K. Leinlogel, L.J. Gauckler, *Solid State Ionics* 135 (2000) 567–573.
- [23] T.S. Zhang, J. Ma, S.H. Chan, J.A. Kilner, *J. Electrochem. Soc.* 151 (10) (2004) J84–J90.